All-dielectric nanophotonics: the quest for better materials and fabrication techniques

Review Article Vol. 4, No. 7 / July 2017 / Optica 814

All-dielectric nanophotonics: the quest for better materials and fabrication techniques

Denis G. Baranov,[1,2,*,†] Dmitry A. Zuev,[3,†] Sergey I. Lepeshov,[3] Oleg V. Kotov,[4] Alexander E. Krasnok,[3,5] Andrey B. Evlyukhin,[3,6] and Boris N. Chichkov[6,7]

[1]Department of Physics, Chalmers University of Technology, 412 96 Gothenburg, Sweden
[2]Moscow Institute of Physics and Technology, Dolgoprudny 141700, Russia
[3]ITMO University, St. Petersburg 197101, Russia
[4]N. L. Dukhov Research Institute of Automatics, Moscow 127055, Russia
[5]Department of Electrical and Computer Engineering, The University of Texas at Austin, Austin, Texas 78712, USA
[6]Laser Zentrum Hannover e.V, 30419 Hannover, Germany
[7]Leibniz Universität, 30167 Hannover, Germany
*Corresponding author: denisb@chalmers.se

Received 1 February 2017; revised 12 June 2017; accepted 17 June 2017 (Doc. ID 285622); published 17 July 2017

All-dielectric nanophotonics is an exciting and rapidly developing area of nano-optics that utilizes the resonant behavior of high-index low-loss dielectric nanoparticles to enhance light–matter interaction at the nanoscale. When experimental implementation of a specific all-dielectric nanostructure is desired, two crucial factors have to be considered: the choice of a high-index material and a fabrication method. The degree to which various effects can be enhanced relies on the dielectric response of the chosen material as well as the fabrication accuracy. Here, we provide an overview of available high-index materials and existing fabrication techniques for the realization of all-dielectric nanostructures. We compare performance of the chosen materials in the visible and IR spectral ranges in terms of scattering efficiencies and Q factors of the magnetic Mie resonance. Methods for all-dielectric nanostructure fabrication are discussed and their advantages and disadvantages are highlighted. We also present an outlook for the search for better materials with higher refractive indices and novel fabrication methods that will enable low-cost manufacturing of optically resonant high-index nanoparticles. We believe that this information will be valuable across the field of nanophotonics and particularly for the design of resonant all-dielectric nanostructures.

OCIS codes: (160.4760) Optical properties; (160.6000) Semiconductor materials; (220.4241) Nanostructure fabrication; (350.4238) Nanophotonics and photonic crystals.

https://doi.org/10.1364/OPTICA.4.000814

1. INTRODUCTION

Plasmonics, the study of extraordinary optical properties of metallic nanoparticles, has been the avant-garde of nanophotonics for more than a decade. The intense research in this field has arisen due to the ability of nanoparticles made of noble metals (gold, silver) to enhance the electromagnetic field on the nanoscale, enabling unprecedented opportunities for boosting various optical effects and manipulation of electromagnetic radiation in unusual ways [1–6]. However, the high level of Joule losses associated with the free electron response of noble metals was always a challenge limiting the efficiency of optical devices [7–9]. Although certain loss-compensation approaches for plasmonic nanostructures based on gain media [10–15] and a very special configuration of the metal conduction band [16] have been suggested, their versatile implementation has proven to be challenging. As a result, the problem of Joule damping has motivated researchers to search for alternatives to noble metals, such as heavily doped semiconductors [17] and polar crystals exhibiting Reststrahlen bands [18].

Mie resonances of *high-index dielectric nanoparticles* pave an alternative route toward the development of nanostructures with special optical properties. Although the Mie theory predicting the resonant behavior of high-index subwavelength particles has existed for more than a century [19], the enormous interest in optical properties of all-dielectric nanostructures has arisen only recently with observation of low-order Mie modes in silicon colloids [20,21] and thanks to the advances in fabrication of single dielectric nanoparticles with a controlled geometry [22–26]. Resonant behavior of high-index nanoparticles not only enables realization of low-loss nonplasmonic metamaterials and metasurfaces [27–30] with rich optical functionalities [31–36], but also paves the way to enhanced light–matter interaction [37–40] as well as advanced linear [41–49] and nonlinear [50–53] light manipulation.

All-dielectric nanophotonics offers a variety of intriguing optical effects and enables promising practical applications [26,47,54]. In order to implement these possibilities, *materials with specific optical*

properties are desired, and certain *fabrication methods* must be available. Although the technologies of manufacturing of silicon particles are well established today [54], silicon is not the only candidate for high-index Mie resonators. There is a plethora of semiconductors and polar materials exhibiting attractive characteristics in visible and infrared (IR) spectral regions in the context of all-dielectric nanophotonics. Here, we present a comparative analysis of available high-index materials in view of their performance as optical nanoresonators. The resonant behavior is analyzed in terms of linear characteristics of spherical nanoparticles. To complement this analysis, we review the existing fabrication methods of nanostructures from various high-index materials. Finally, we provide motivations for the search for better materials with higher refractive indices and novel fabrication methods, enabling low-cost manufacturing of optically resonant dielectric nanoparticles.

2. OVERVIEW OF HIGH-INDEX MATERIALS

A. Scattering by Plasmonic and Dielectric Nanoparticles

To set the stage, let us recall the basics of light scattering by spherical particles. The electromagnetic response of a spherical particle made of material with permittivity ε of any size is exactly described by the Mie theory [19]. In this framework, the electromagnetic field scattered by a sphere is represented as a sum of electric-type (TM) and magnetic-type (TE) spherical harmonics. Amplitudes of these harmonics are expressed by the Mie coefficients a_n for the electric modes and b_n for the magnetic modes. Each of these amplitudes has a set of resonance frequencies at which the electromagnetic field of the corresponding harmonic is enhanced both inside and outside of the sphere.

An enhancement of optical phenomena by resonant nanostructures can be described with various figures of merit. In the context of spectroscopic applications, the local electric field enhancement is the crucial parameter that defines the efficiency of such processes as spontaneous emission, Raman scattering, higher harmonics generation, and others [55–57]. Using the temporal coupled-mode theory, the local field enhancement (averaged over the mode volume) may be expressed as follows [58]:

$$\left(\frac{E_{\text{loc}}}{E_{\text{inc}}}\right)^2 \propto \gamma_{\text{rad}} \frac{Q^2}{V}, \tag{1}$$

where $Q = \omega/(\gamma_{\text{rad}} + \gamma_{\text{nrad}})$ is the quality factor of the excited mode; γ_{rad} and γ_{nrad} are the nanoantenna radiative and nonradiative decay rates, respectively; V is its mode volume. Equation (1) suggests that high Q and small V are beneficial for the local field enhancement with nanoantennas.

In contrast to plasmonics, where the Joule losses represent the dominant dissipation channel, the Q factor of high-index Mie resonators is mainly limited by the radiation damping. In the context of metasurfaces, which manipulate the characteristics of propagating fields, radiation should not be treated as a loss. For this reason, a relevant figure of merit is the nanoantenna radiation efficiency η_{rad},

$$\eta_{\text{rad}} = \frac{\sigma_{\text{scat}}}{\sigma_{\text{scat}} + \sigma_{\text{abs}}}, \tag{2}$$

with σ_{scat} and σ_{abs} being the scattering and absorption cross sections, respectively. A value of η_{rad} close to 1 indicates that almost all incident light is reradiated without being absorbed by nanoantennas, constituting a metasurface. At the same time, a smaller nanoantenna size is also desired, since it would allow smaller distances between neighboring nanoantennas, reducing the spatial dispersion effect.

The extraordinary enhancement of an electric field by plasmonic nanoparticles relies on the free electron response; Fig. 1(a). When the frequency of incident light matches that of the free electrons' oscillations inside a sphere, the plasmonic resonance manifests itself and a strong electric field is produced in the vicinity of the particle. These oscillations, however, are accompanied by significant optical loss arising from both intraband and interband transitions and eventually heat the particle [9]. In contrast, optical resonances of high-index nanoparticles originate from the *displacement currents* due to oscillations of bounded electrons; Fig. 1(a). These currents are free of Ohmic damping, which allows us to reduce the nonradiative losses and heating of the optical nanoresonator.

Of special interest to the field of nanophotonics is the *magnetic dipole (MD) resonance* of high-index nanoparticles—the fundamental magnetic dipolar mode of a dielectric sphere. At a fixed nanosphere diameter, the MD resonance occurs at the smallest frequency of the incident wave compared to other resonances [22,31]. Besides being the lowest-energy Mie resonance of a nanosphere, the MD resonance exhibits stronger enhancement of spontaneous emission and nonlinear effects than the electric dipole resonance due to larger local field enhancement and local density of states [39,50,59,60]. For this reason, below we will focus on the features of the MD mode.

The spectral position of the MD resonance of a spherical particle is approximately defined by $\lambda_{\text{MD}} \approx nD$ with n being the refractive index of the sphere and D its diameter [22,23]. Therefore,

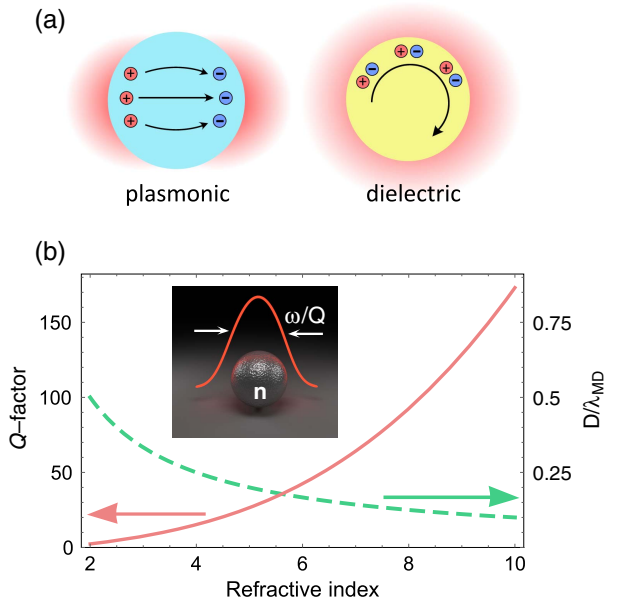

Fig. 1. (a) Schematic illustration of fundamental resonances and induced currents in plasmonic and dielectric nanoparticles. Free electrons of the metal give rise to the conduction currents in plasmonic nanoparticles, while bounded charges in dielectrics cannot move freely across the particle and give rise to the displacement currents. (b) Refractive index dependence of the Q factor of the magnetic dipole resonance of a spherical nanoparticle and the respective dependence of the resonant nanoparticle diameter D. The nanoparticle size is continuously tuned such that is satisfies the MD resonance condition at each point.

larger refractive indices are desirable from the point of view of device miniaturization. The field enhancement and Q factor of Mie resonances also benefit from the large particle refractive index [see Fig. 1(b)]—this may be intuitively understood as the result of smaller radiation leakage from nanoparticles with a larger refractive index contrast.

B. High-Refractive-Index Materials

The above considerations clearly pose the *quest for materials* with large refractive indices. In the visible and near-IR spectral ranges, the highest known permittivities are demonstrated by semiconductors such as Si, Ge, GaSb, and others; see Fig. 2(a). In the neighboring mid-IR range, which is also of great interest to optoelectronic technology, narrow-band semiconductors and polar crystals demonstrate very attractive characteristics, and have been implemented for the design of all-dielectric metamaterials consisting of resonant Te [30] and SiC [29] elements.

The origin of the relatively high refractive index of these materials can be understood from the picture of their electronic response depicted in Fig. 2(b), which shows the refractive index of a generic material possessing interband and phonon resonances represented as two Lorentzians. While in the low-frequency regime the response is purely dielectric (assuming that the material is not doped with free carriers), in the IR and visible spectral ranges these materials exhibit a series of resonances. Due to the coupling of light to these resonances of the medium, the regions of increased refractive index appear in the spectrum. The low-frequency phonon–polariton resonance occurs due to the coupling of light with optical phonons of the crystal lattice of polar crystals [61,62]. The higher-frequency exciton–polariton resonance originates from interband transitions in semiconductors and forms a pronounced plateau in their dielectric function. As Fig. 2(c) shows, real semiconductors and polar materials indeed demonstrate qualitatively similar dispersions of the refractive index.

The high refractive index of these materials comes at a cost of increased absorption. According to the Kramers–Kronig relations [63], any dispersion of permittivity is related to dissipation. As it was pointed out above, the high-index regions of semiconductors and polar crystals stem from their exciton and phonon resonances, which bring optical absorption. This fundamental trade-off between absorption and high refractive index eventually sets the limit to all-dielectric resonator performance.

There is a significant difference between the behavior of refractive indices of semiconductors and polar crystals. In semiconductors, the high refractive index at below-band gap frequencies originates from a continuum of interband transitions [62], which allows one to have a high index and a relatively low absorption at the same time. In polar crystals, the high index is related to a single phonon resonance, so that it is accompanied by a large absorption coefficient [64].

The value of the refractive index of a semiconductor is closely related to its electronic band gap. Generally, the *electrostatic* refractive index of a semiconductor decreases with the increasing energy gap. This correlation can be understood from the following argument, suggested by Moss [65]. He considered electrons in a semiconductor as if they were bound to a hydrogen atom. The energy needed to ionize the atom and to raise an electron to the conduction band scales is $E_g \sim 1/\varepsilon^2$, where ε is the background (electrostatic) permittivity of the semiconductor. This results in a very simple approximation for the static refractive index known as the Moss formula,

$$n^4 E_g = 95 \text{ eV}. \tag{3}$$

There are several other models leading to similar dependencies [66,67]. Although being valid for static permittivity, this approximation qualitatively reproduces the behavior of refractive indices at optical and IR wavelengths, as summarized in Fig. 2(a): overall, narrow-gap semiconductors such as PbTe, GeTe demonstrate higher refractive indices than those with an energy gap lying in the visible range. Detailed information on the optical properties of chosen materials, including values of the extinction coefficients and electronic band gap as well as the sources from which the data on permittivity dispersion derives, is presented in Table 1.

Semiconductor materials may have either a direct or indirect band gap, which has a profound implication on the absorbing properties. When light passes through a direct-band-gap semiconductor, a photon can be absorbed to the conduction band. At the same time, when light travels through an indirect-band-gap medium, due to the large mismatch between the electron and photon wavevectors, such process does not occur, which results in reduced optical absorption. Good examples of such materials are c-Si and Ge. Nevertheless, even direct-band-gap materials may demonstrate good performance if the operation frequency lies slightly below the band gap.

C. Comparative Analysis of Materials

Let us now illustrate the performance of the available high-index materials for the case of a spherical particle, since it allows an exact analytical solution. First, we present in Figs. 3(a)–3(c) the Q factor of the MD resonance of a spherical particle as a function of

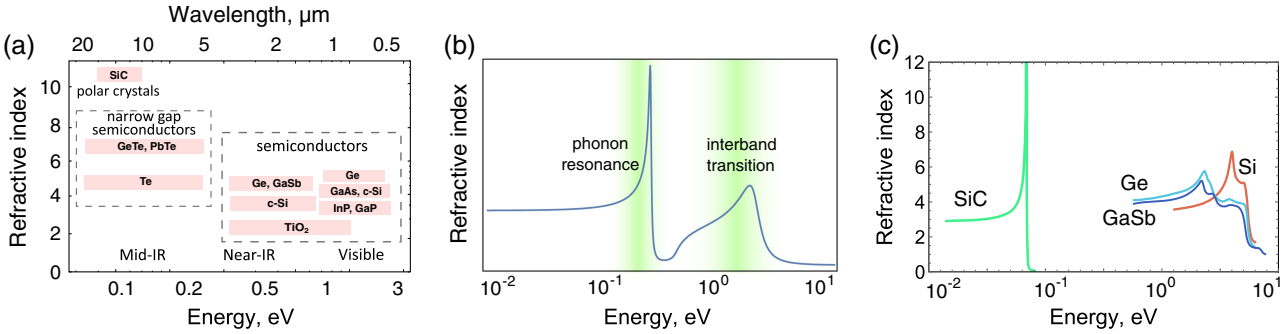

Fig. 2. (a) Refractive indices of materials available for dielectric nanophotonics from visible to mid-IR spectral ranges. (b) A typical dielectric response of a high-index material exhibiting a series of resonances. Shaded area depicts two high-index plateau related to material resonances. (c) Refractive index of several semiconductors, and SiC showing behavior very similar to that of the generic material shown in (b).

Table 1. Optical Properties of Selected High-Index Materials

Material	Spectral Range, μm	Refractive Index, n	Extinction Coefficient, k	Band Gap Type	Band Gap Energy, eV	References
c-Si	0.50–1.45	4.293–3.486	0.045–0.001	indirect	1.12	[68]
	1.45–2.40	3.484–3.437	~0			[69]
a-Si	0.50–1.00	4.47–3.61	1.12–0.01	indirect	1.50	[70]
GaAs	0.50–0.80	4.037–3.679	0.376–0.089	direct	1.46	[71]
GaP	0.50–0.80	3.590–3.197	~0	indirect	2.26	[71]
InP	0.50–0.80	3.456–3.818	0.203–0.511	direct	1.27	[72]
TiO_2	0.50–1.00	2.715–2.483	~0	indirect	3.05	[73]
Ge	0.50–0.60	4.460–5.811	2.366–1.389	indirect	0.67	[71]
	0.60–0.80	5.811–4.699	1.389–0.3			
	0.80–1.90	4.684–4.129	0.3–0.001			[74]
	1.90–2.40	4.111–4.069	~0			[69]
GaSb	1.00–2.40	4.140–3.846	0.225–0.001	direct	0.69	[75]
Te	4.00–14.0	4.929–4.785	~0	indirect	0.34	[76]
PbTe	4.10–12.5	5.975–5.609	~0	direct	0.31	[77]
GeTe[a]	6.20–11.8	7.3–7.278	~0	direct	0.2	[78]
SiC	11.0–15.0	~20	~15	—	—	[79]

[a]Theoretical values of the refractive index are quoted for GeTe.

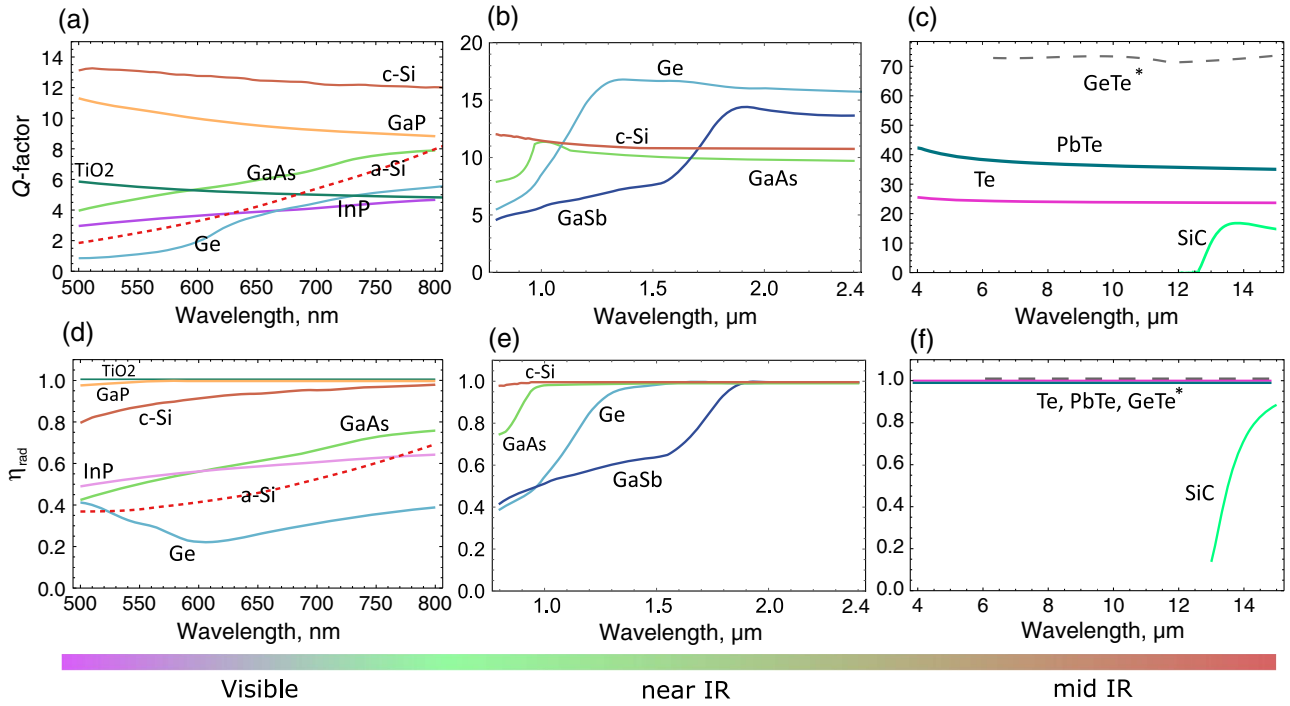

Fig. 3. Quantitative comparison of the available high-index materials for all-dielectric nanophotonics. (a)–(c) Q factors of the magnetic dipole (MD) resonance of spherical nanoparticles made of various high-index materials as a function of wavelength in the (a) visible, (b) near-IR, and (c) mid-IR regions. The nanosphere sizes were continuously tuned in such a way that they satisfy the MD resonance condition at each wavelength. GeTe is marked with * because theoretical values of refractive index were used to calculate the response of GeTe nanoparticles. (d)–(f) The antenna radiation efficiency η_{rad} at the MD resonance for the same scope of materials.

wavelength. In order to obtain this dependence, we continuously tune the nanoparticle size such that is satisfies the MD resonance condition at each wavelength. The Q factor was obtained by calculating the full width of the MD resonance scattering cross section. The results show that across the whole visible spectral range among all semiconductors, c-Si demonstrates the highest Q factor of around 13, with the closest being GaP, with a Q factor of only around 10. The good performances of c-Si and GaP are caused by the fact that these two materials are indirect-band-gap semiconductors, which results in the reduced optical absorption and therefore higher Q factors.

In the near-IR region, Ge takes the pedestal with a Q-factor slightly above 15 at the most interesting wavelength of 1.55 μm; Fig. 3(b). A remarkable "jump" of Q factors of Ge, GaSb, and GaAs nanoparticles occurs at wavelengths just slightly longer the onset of the direct transition, which is in excellent agreement with our previous argument that direct-band-gap semiconductors may demonstrate favorable characteristics. In the mid-IR, the situation is strikingly different: particles of narrow-band-gap semiconductors PbTe and GeTe demonstrate Q factors well above 40 and 70, respectively. We note here that the values for GeTe quoted in Table 1 are obtained from the theoretical calculations

of Ref. [78]. Therefore, superior values for GeTe may be lower in reality. Nevertheless, GeTe demonstrates the highest Q factor among all selected materials, which makes it very attractive for more detailed study. SiC, on the other hand, despite its huge refractive index exceeding 10, shows a very low quality factor. Such poor optical response of SiC nanoparticles stems from narrow phonon resonance of the polar crystal associated with large absorption, as argued above.

The results presented in Figs. 3(d)–3(f) indicate that the radiation efficiencies of semiconductor nanoparticles η_{rad} calculated with Eq. (2) generally increase with the increasing wavelength. Interestingly, in the visible range the highest radiation efficiency is demonstrated by TiO_2 and GaP nanoparticles due to the widest electronic band gap and thus the smallest absorption among the studied materials; see Table 1. In the near-IR, the efficiency of Ge and Si antennas is nearly 1 at wavelengths longer than 1.5 μm. In the mid-IR, the efficiencies of Te, PbTe, and GeTe particles are equal to 1, while SiC particles show very poor performance with low radiation efficiency and Q factor owing to the sharp phonon resonance.

Although the spherical geometry of a particle is attractive from the theoretical standpoint, as it allows exact analytical description of light scattering, fabrication of spherical particles is not always an option. On the other hand, Mie resonances occur for a wide range of particle shapes, including nanodisks, which may be easily fabricated by the standard nanolithography techniques (see Section 3.A) for any material considered in this study. For this reason, we performed the same analysis of Q factors for nanodisks made of different materials. The results shown in Fig. 4 demonstrate that behavior of Q factors is overall similar to that observed for spherical particles. To conclude this section, we finally note that the observed Q-factor values do not set the upper limit for high-index nanostructures, and larger Q factors can be obtained in clusters of nanoparticles, such as dimers and metasurafces [34,80,81], and structures supporting a Van Hove singularity [40].

3. OVERVIEW OF FABRICATION TECHNIQUES

Bearing in mind the above considerations about high-index materials, we may now proceed to a brief review of the existing fabrication techniques. The rapid progress of nanotechnology has enabled tremendous development of methods for semiconductor nanoparticle fabrication. The most illustrative example is presented by silicon, since it is the most frequently used high-index material in the visible and IR ranges owing to its relatively low cost and low imaginary part of the refractive index [54]. Therefore, it is not surprising that methods of fabrication of silicon nanostructures have been the first historically proposed. Initially, different methods for fabrication of optically small and nonresonant silicon nanoparticles were developed basically for biological imaging and drug delivery [82], including methods of mechanical milling [83], pulsed laser ablation in liquid [84], electrochemical etching [85], gas phase synthesis [86], among others.

In the context of nanophotonic applications, nanoparticles with the magnetic and electric resonances located in the visible or near-IR spectral regions are desired. This requirement sets up high demands not only for the nanoparticle size, but also for repeatability and throughput of fabrication methods, precise control of nanoparticle geometry, simplicity of the fabrication procedure (quantity of steps involved in the fabrication process), and manipulation of nanoparticle space arrangement. Therefore, the development of fabrication technologies of Mie-resonant high-index nanoparticles has recently been initiated that resulted in the emergence of various techniques, summarized in Fig. 5 in terms of five representative parameters: repeatability, productivity, resolution, positioning control (possibility to place a nanostructure at a certain position immediately during fabrication), and method complexity.

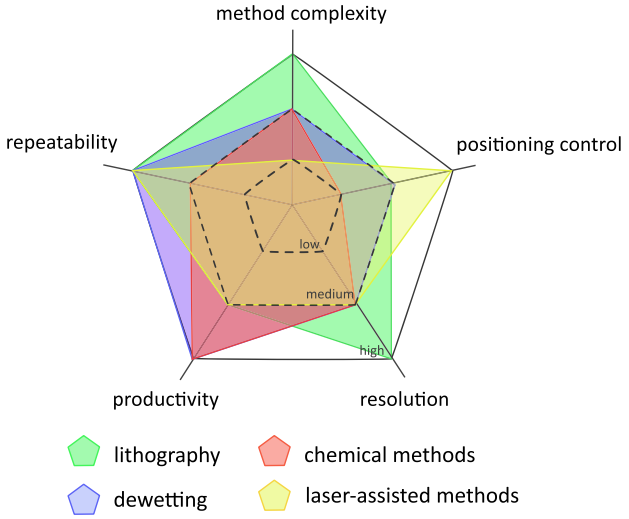

Fig. 5. Schematic comparison of fabrication techniques of high-index nanostructures.

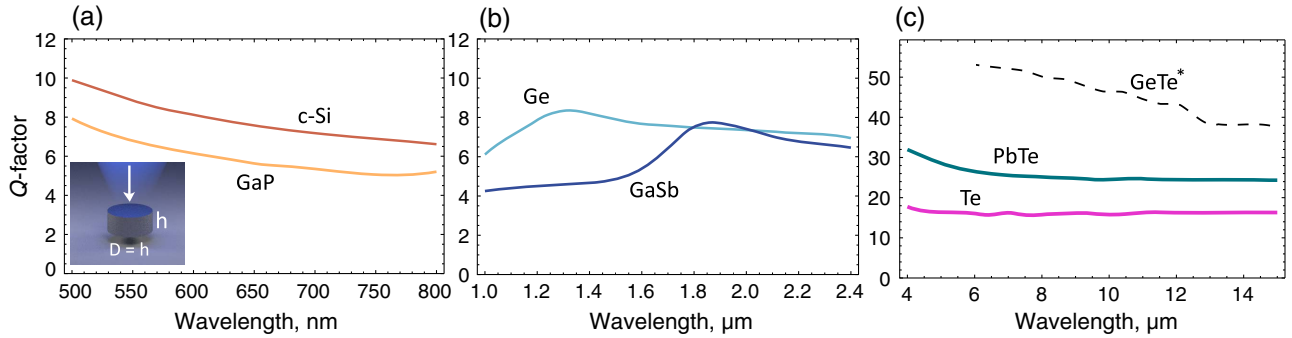

Fig. 4. Q factors of the MD resonance of nanodisks with equal height and diameter. The nanodisk sizes were continuously tuned in such a way that they satisfy the MD resonance condition at each wavelength.

This picture demonstrates that all techniques have inherent advantages and disadvantages. Thus, the choice of a fabrication method of high-index nanoparticles is determined by the objectives of the investigation, e.g., in case of high demands to chemical purity and the need to place nanostructures in different areas of the substrate during fabrication, laser-assisted methods are preferable. In contrast, if high productivity is a cornerstone, chemical methods will be considered as more preferable ones. To better understand the applicability of these methods for a special case, they should be carefully considered on the example of fabricated high-index nanostructures.

A. Lithography

1. Single Nanostructures

The most straightforward methods for fabrication of nanostructures involve lithography, since it provides high repeatability alongside an opportunity to fabricate nanostructures of complicated shapes via a combination of lithographic processes. The conventional lithographic methods have been successfully applied for the fabrication of single nanoparticles of different shapes. For example, silicon nanoresonators consisting of hollow nanocylinders with an outer diameter of 108–251 nm and a gap in the center diameter of >20 nm were fabricated by the combination of electron-beam lithography with reactive-ion etching; Fig. 6(a) [87]. The geometry of these structures (the outer diameter, height, and wall thickness) can be varied to control the resonant wavelength and relative spectral spacing and composition of the modes.

In Ref. [88], a single dielectric nanorod antenna [see Fig. 6(b)] consisting of amorphous alloys of C and O was fabricated via electron-beam-induced deposition. The control of nanoantenna geometry via fabrication process was applied for resonant light scattering manipulation over the whole visible wavelength range. In Ref. [89], the intersection region of two silicon waveguides was replaced by an array of silicon cylinders; Fig. 6(c). The proposed method of high-index nanostructure fabrication is very promising for optical cross-connects because the cylindrical shape of nanoparticles is compatible with the existing lithography processes, and can be fabricated synchronously with waveguide components.

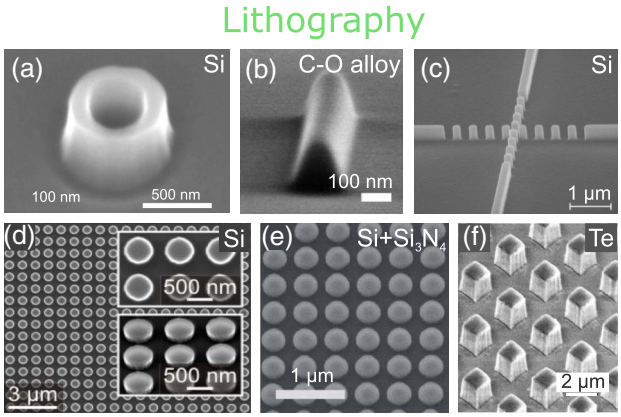

Fig. 6. Examples of high-index dielectric nanostructures fabricated by lithography. (a) Scanning electron microscopy (SEM) image of hollow Si cylinder. (b) SEM image of carbonaceous dielectric nanorod antenna fabricated by electron-beam-induced deposition. (c) Periodic dielectric waveguide crossing. (d) Silicon nanoparticles obtained by means of reactive-ion-etching through a mask. (e) Si nanoparticles with additionally deposited Si_3N_4 thin film. (f) High-index cubic tellurium resonators. Reprinted with permission from: (a) Ref. [87], (b) Ref. [88], (c) Ref. [89], (d) Ref. [90], (e) Ref. [91], (f) Ref. [30].

2. Nanostructure Arrays

The standard micro/nanofabrication processing techniques are proven to be effective in terms of large-scale nanostructure array fabrication. This is very important for the creation of high-index metasurfaces setting higher demands for the precision and reproducibility of nanostructures. The controllable fabrication of silicon nanoparticle arrays was achieved by a multistep method, including electron-beam lithography on silicon-on-insulator wafers (formation of mask from resist) and the reactive-ion-etching process with following removal of remaining resist mask. This technology allows the formation of arrays of silicon nanodisks [Fig. 6(d)], in which Mie resonances can be precisely tuned by variation of their geometrical parameters [90]. More complicated nanostructures representing the combination of Si nanoparticles with an Si_3N_4 layer were realized by Spinelli *et al.*; see Fig. 6(e). Si nanoparticles were produced on the silicon wafers by substrate conformal soft-imprint lithography in combination with reactive-ion etching. The nanostructures fabricated by this technology demonstrate the average reflectivity reduction up to values lower than 3% over the wide spectral range of 450–900 nm. Finally, fabrication of more sophisticated chiral Si nanoparticles via anisotropic etching has been recently demonstrated by Verre *et al.* [92].

Multistep lithography methods have been also implemented for the fabrication of high-index tellurium dielectric resonators for all-dielectric metamaterials; Fig. 6(f) [30]. The BaF_2 optical flat substrate was applied for deposition of 1.7 μm Te thick film by electron-beam evaporation. Then, this film was patterned using electron-beam lithography and a reactive-ion etching process to fabricate the uniform structure. Zero backscattering and significant light dispersion in the forward direction were demonstrated for GaAs nanoparticles, fabricated with molecular beam epitaxy, lift-off procedure, reactive-ion and plasma etching with a flip-chip bonding process [93].

GaAs metasurfaces represent a great deal of interest because of the beneficial optoelectronic properties. Recently, a few lithographic processes for GaAs metasurfaces have been demonstrated [94,95], including selective wet oxidation, where GaAs metasurfaces were fabricated using a combination of high-aspect-ratio etching and selective wet oxidation of AlGaAs underlayers [96]. This approach provides a low-refractive-index native oxide layer between the resonators and the semiconductor substrate and was adapted for creation of a multilayer GaAs metamaterial structure providing a reflectivity value exceeding that of gold over a broad spectral range. The multistep lithography methods are also attractive for other materials.

Fabrication of a Te dielectric metamaterial structure was demonstrated by Liu *et al.* [97] using multicycle deposition-etching-liftoff technique. Polman and colleagues fabricated an array of TiO_2 nanostructures on a Al_2O_3-passivated Si wafer by a combination of standard lithography methods: substrate-conformal imprint lithography, reactive-ion etching, and plasma-assisted atomic layer deposition (ALD) [98]. These procedures made possible fabrication of nanopatterned dielectric coating for crystalline Si solar cells possessing antireflection properties due to preferential forward scattering of light via proper engineering of Mie resonances of TiO_2 nanocylinders. The combination of e-beam lithography and dielectric reactive-ion etching was also successfully implemented in metasurface design,

demonstrating a Q factor of 350 (for the Si-based structure) and 600 (for the GaAs-based structure) in the near-IR (1 μm) [81].

Another approach to fabrication of planar optical metasurfaces based on high-quality TiO_2 grown by ALD has been demonstrated by Capasso and colleagues [35,99] (see also Ref. [100] for a review of planar optical metasurfaces). Here, ALD provides precise control of film thickness (up to a monolayer) and the material phase, making possible creation of high-aspect-ratio nanostructures with no losses in the visible region. The proposed approach can be applied to any type of metasurface.

Thus, lithographic methods remain more reliable for high-index nanostructure fabrication combining three important qualities: high reproducibility for the nanostructure arrays, an ability to fabricate the nanostructures with complex shape, and high resolution. More information on lithographic fabrication of dielectric nanostructures can be found in Ref. [101]. It should be mentioned that in spite of these advantages, the lithography methods can hardly be applied for the creation of spherical nanoparticles, which represent interest not only for fundamental but also for applied sciences. Moreover, the multiple steps that are often required for high-index nanostructure fabrication, as well as the complexity and high cost of equipment motivate researchers to look for novel fabrication methods.

B. Chemical Methods

Chemical methods are promising in terms of high-throughput fabrication of nanoparticles. These methods also offer flexibility in synthesis of materials, relative simplicity, and compatibility with other methods of solid material synthesis. One of the most widespread methods is the chemical vapor deposition technique. This process can be applied as an effective method for the fabrication of silicon nanoparticles with different sizes: e.g., fabrication of silicon nanoparticles can be carried out by decomposition of disilane gas (Si_2H_6) at high temperatures into solid silicon and hydrogen by the following chemical reaction: $Si_2H_6 \rightarrow 2Si(s) + 3H_2(g)$. As a result, spherical polydisperse silicon particles with diameters from 0.5 to 5 μm [20] and about 300–500 nm [102] were produced by this method. The decomposition temperature of the precursor as well as annealing treatment can be chosen to fabricate amorphous or polycrystalline particles with a crystallite size of about 3 nm. It is interesting that the appearance of unwanted silicon dust in the decomposition of silicon precursors was mentioned long before the rise of dielectric nanophotonics [103]. This dust is in fact composed of silicon nano- and microspheres [20,102].

The crystalline silicon Mie resonators can be also created via alkaline chemical etching combined with electronic lithography [104]. This method eliminates reactive-ion etching and can be applied for the fabrication of both silicon nanoresonators and oligomers. Further, fabrication of a monodispersed silicon colloid was achieved via decomposition of trisilane (Si_3H_8) in supercritical n-hexane at high temperature [105]. In this method, the particles size can be controlled by changing the trisilane concentration and reaction temperature. Large ensembles of similar silicon nanoparticles with size dispersion in the range of several percents, which can be ordered into hexagonal lattice by self-assembly [Fig. 7(a)], can be obtained. The main disadvantage of this technique is the porosity and high hydrogen content of nanoparticles, as well as the necessity of additional patterning methods to fabricate functional structures.

The chemical procedures can be easily combined with lithography. Brongersma and colleagues implemented the combination of lithography and oxidization in air for fabrication of a periodic

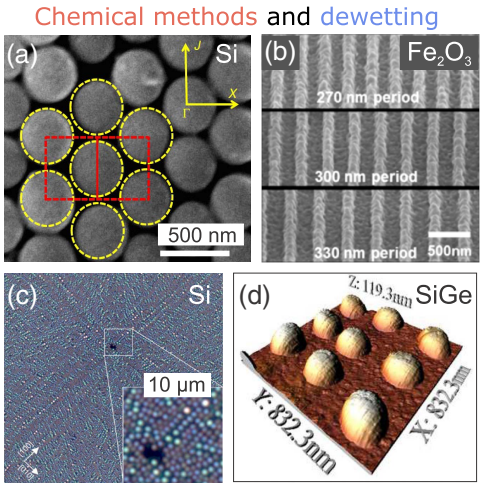

Fig. 7. Examples of high-index dielectric nanostructures fabricated by chemical methods and dewetting. (a) Self-aligned silicon nanoparticles obtained by chemical deposition. (b) Periodic Fe_2O_3 nanobeam-array with different periods fabricated via combination of lithography (top image) and oxidation in air (bottom). (c) Dark-field optical image of silicon nanoparticles obtained by thin film dewetting. (d) AFM image of SiGe islands in array received after thermal dewetting. Reprinted with permission from: (a) Ref. [105], (b) Ref. [106], (c) Ref. [107], (d) Ref. [108].

Fe_2O_3 nanobeam array for active photocatalytic material creation supporting optical Mie resonances; Fig. 7(b) [106]. Chemical methods can also be combined with standard commercial products to generate nanostructures for new dielectric metamaterial designs, e.g., SiC nanorods available commercially were washed in ethanol and studied [29]. Lewi *et al.* fabricated tunable chemically synthesized PbTe cubic resonators demonstrating ultra-wide dynamic tuning [109] by a facile alkaline hydrothermal method [110].

Thus we may conclude that, although the inherent disadvantages (chemical waste, possible contamination of fabricated nanomaterials, additional steps for generation nanostructures, etc.) impose constraints on the possible application areas, the chemical methods provide large opportunities for researchers.

C. Dewetting

Dewetting of a thin film is another process that can be applied for fabrication of high-index nanoparticles on a large scale. This process implies agglomeration of nanoparticles during heating of a thin film due to minimization of total energy of the thin film surfaces, including a film–substrate interface [111,112]. The film thickness has a direct influence on the dewetting process (the lower the thickness, the higher the driving force for dewetting) [112], therefore dewetting can be carried out at temperatures lower than the melting threshold of the thin film material. Overall, the main controlling parameters in this method are the heating temperature and properties of the thin film (thickness, presence of defects, and initial patterns).

Dewetting has been applied for the fabrication of silicon nanoparticles with different sizes after heating of thin crystalline [107] or amorphous [113] silicon films. This method also enables a controlled formation of complex assemblies of silicon monocrystalline resonators; Fig. 7(c) [107]. It should be noted that in the thin film dewetting technique the nanoparticle size and location control can be achieved only by using additional lithographic

methods, which is even more complicated compared to the chemical deposition techniques.

In spite of this fact, dewetting offers great opportunities in terms of productivity and can be applied to any material. Appropriate choice of the substrate temperature during the growth process provides an effective approach for the creation of needle-like Te crystallites [114]. In Ref. [115], two-component SiGe nanoparticles were obtained after thermal dewetting. In this work, thermal dewetting and agglomeration of the Ge layer deposited on a 9 nm thick Si (001) layer was investigated. It was demonstrated that Ge layer lowers the dewetting temperature and makes possible the creation of SiGe nanoparticles. SiGe nanostructures were also fabricated by focused ion beam templating followed by thermal dewetting; see Fig. 7(d) [108]. This approach made possible fabrication of resonator arrays in a large scale functioning as color pass-band filters across the full visible spectral range.

Thereby, dewetting is a simple and highly productive method for the fabrication of high-index nanoparticles. However, the controllable arrangement of nanoparticles in certain places on the sample surface is still a problem for this method.

D. Laser-Assisted Methods

Fast progress in nanotechnologies demands growing precision of fabrication processes. It is not surprising that laser-assisted methods are applied in different nanofabrication processes due to their material selectivity, submicron resolution, high energy density, etc. For example, laser-assisted methods were proven to be effective for the fabrication of nanoparticles with diameters less than 100 nm. It is worth noting that colloids of chemically pure nanoparticles can be obtained by means of laser ablation in liquids. The main advantages of the ablation approach are relatively high productivity and lack of harmful chemical wastes.

The growing interest in the fabrication of high-index nanoparticles stimulated application of laser-assisted methods for the generation of nanoparticles with sizes larger than 100 nm supporting Mie resonances in the visible and near-IR regions. Studies in this field have only recently begun, and laser-assisted methods have been applied mostly to silicon.

1. Ablation of Bulk Materials

The first experiments towards fabrication of high-index nanoparticles using laser-assisted methods were conducted by direct laser ablation: an ultrashort-laser-pulse-induced material fragmentation into spherical nanoparticles and their deposition close to the focus area; Fig. 8(a) [22,23,46,120,121]. Laser ablation in superfluid helium was also successfully implemented for the fabrication of single-crystalline sub-micron- and micron-sized ZnO, CdSe, ZnSe, and CeO_2 microspheres, Figs. 8(b) and 8(c) [117]. These experiments proved the effectiveness of laser ablation for the fabrication of high-index nanoparticles with optical response (scattering efficiencies, Q factors, etc.) in the visible and IR spectral ranges. Laser ablation of the target wafer for fabrication of PbTe Mie spherical resonators was also utilized by Lewi *et al.* [109]. These nanoresonators demonstrate high-quality-factor Mie-resonances that can be tuned by small temperature modulation. However, application of such processes in nanophotonics is a problem due to the inability to control the fabricated nanoparticle sizes and their locations. To overcome these problems, other laser-assisted methods were developed.

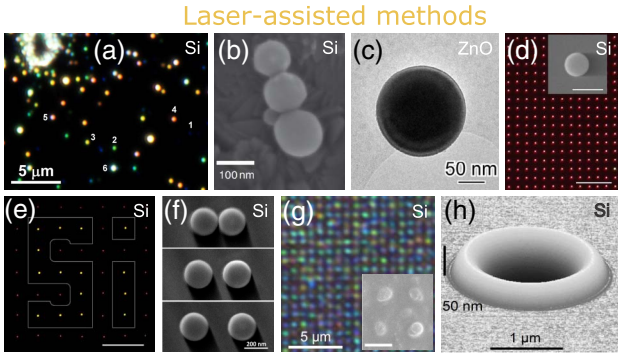

Fig. 8. Examples of high-index dielectric nanostructures fabricated by laser assisted methods. (a) Dark-field optical image of silicon nanoparticle obtained via femtosecond laser ablation of bulk silicon. (b) SEM image of a silicon nanosphere trimer. (c) TEM image of a ZnO submicrosphere. (d)–(e) Demonstration of the laser-printing method: (d) array of amorphous Si nanoparticles fabricated by LIT method and visualized with dark-field microscopy (scale bar, 20 μm). The insert shows a SEM image of a single Si nanoparticle in this array (scale bar, 200 nm). (e) Dark-field optical image of silicon nanoparticles obtained via femtosecond laser ablation of thin silicon film. In picture (e) red nanoparticles are amorphized, while yellow are annealed and crystalline. (f) SEM images of Si nanoparticle dimer structures on a glass substrate. (g) Optical image of an array of the silicon nanoparticles fabricated by direct laser writing; inset displays SEM image of the written nanoparticles covered by a 10 nm gold layer with the scale bar of 700 nm. (h) AFM image of typical laser dimples on c-Si. Reprinted with permission from: (a) Ref. [23], (b) Ref. [116], (c) Ref. [117], (d), (e) Ref. [24], (f) Ref. [80], (g) Ref. [118], (h) Ref. [119].

2. Laser-Induced Transfer

Laser-induced transfer (LIT) methods, demonstrated for the first time in the 80s by Bohandy *et al.* [122], have become a promising approach for laser printing of nanoparticles from different materials: metals and semiconductors. In this method, laser radiation is focused on the interface between the printed material and transparent donor substrate providing material transfer onto another receiver substrate placed in close contact with the donor sample. The first experiments on the fabrication of silicon nanoparticles with Mie resonances in the visible range using laser printing were performed by Chichkov and colleagues [24]. With this technique, highly ordered arrays of nanoparticles can be produced [24]; also, dimers consisting of submicron crystalline silicon nanoparticles with different interparticle distances, ranging from 5 to 375 nm, have been demonstrated; Fig. 8(f) [80]. It should be mentioned that laser annealing can be applied for post-processing of laser-printed semiconductor nanoparticles to controllably change their phase from an initially amorphous state to a crystalline state. This allows tailoring their optical properties, e.g., for silicon nanoparticles; Fig. 8(e) [24]. Therefore, the laser-printing technique is very attractive for the fabrication of high-index nanoparticles and their arrangement in 2D arrays with a high precision.

3. Laser-Induced Dewetting

Laser radiation can be applied for patterning of thin films of high-index materials by their controlled dewetting into nanoscale structures. Belov and colleagues demonstrated fabrication of crystalline silicon nanoparticles from amorphous silicon films without applying initially crystalline materials or any additional annealing steps;

see Fig. 8(g) [118]. Laser-based dewetting of amorphous silicon thin films by donut-shaped laser beams was demonstrated in Ref. [123], where morphological modification of the film into a nanodome during thermocapillary-induced dewetting led to phase transformation from amorphous to crystalline structure in the laser focus area. In Ref. [119], dimple-shaped features, which can potentially be applied in nanophotonics, with diameters of 1–4 mm and depths of 1–300 nm were produced on the c-Si surface by nanosecond pulses [Fig. 8(h)].

Thus, laser-assisted dewetting, combining the advantages of dewetting and direct laser patterning, can be considered as a promising method for large-scale fabrication of high-index nanoparticles.

Summarizing this part, it should be noted that laser-assisted methods require high-quality laser radiation (high laser pulse stability, perfect beam shape, and excellent focusing), including high precision and reliability of the position systems. However, these constraints do not lessen the basic advantages of the laser-assisted methods (single-step process, high repeatability, modification of nanoparticles' crystalline phase, space arrangement of the fabricated nanoparticles), which all are important for the realization of nanophotonic devices.

4. DISCUSSION AND OUTLOOK

An overview of the available high-index materials and nanofabrication methods for their potential applications in all-dielectric nanophotonics has been given. Figure 9 briefly summarizes our analysis of high-refractive-index materials. In this plot, materials for which nanoparticle fabrication methods have been demonstrated are highlighted by green color, while materials for which nanofabrication has not yet been demonstrated are highlighted by blue color. Optical performance of each material in terms of the resonance quality factor is determined by the trade-off between the refractive index and related optical absorption.

In the visible region, Si nanoantennas provide the highest field enhancement, while GaP may be preferable for the realization of metasurfaces due to smaller absorption. In the near-IR region, Ge is the best high-index material, while the narrow-band-gap semiconductors, such as GeTe, are more promising for the mid-IR range.

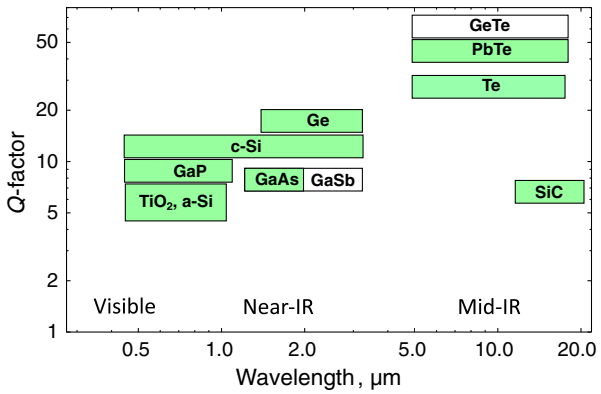

Fig. 9. High-refractive-index materials for all-dielectric nanophotonics: Q factors of spherical resonators made from these materials. Materials that can be nanostructured by the available fabrication techniques are marked by green; nonstructurable materials are marked by blue color.

In terms of nanofabrication, currently developed approaches allow production of different types of all-dielectric functional structures with the desired optical properties. The development of hybrid nanostructures combining plasmonic and Mie resonances will be interesting for different applications in nanophotonics, medicine, ecology, etc.

Further research in this field should be devoted to the search for other materials demonstrating superior behavior in the visible and IR regions. Both direct- and indirect-band-gap semiconductors may turn out to be good candidates for high-index low-loss materials in the visible and near-IR ranges. In the mid-IR range, the ideal high-index material could probably be found among narrow-gap semiconductors.

It is also possible to use gapless direct semiconductors or semimetals, including 3D Dirac semimetals [124–126], where absorption is suppressed due to optical Pauli blocking. However, for applications in the visible range, one needs materials with very high Fermi levels ($E_f > 1$ eV). Optical constants are not determined solely by the electronic band structure; they can be modified by phonon–polariton resonances. These resonances can give a higher refractive index at the cost of increased losses. The large density of phonon modes at room temperature prevents currently known gapless semiconductors and 3D Dirac semimetals from becoming candidates for lossless high-index materials. On the other hand, specific fabrication techniques should be developed to explore the potential of narrow-band-gap semiconductors, such as PbTe and GeTe, as materials for subwavelength mid-IR resonators.

We hope that the provided analysis will serve for better understanding of the design rules of high-index nanoresonators and will facilitate the development of highly efficient optical devices.

Funding. Ministry of Education and Science of the Russian Federation (Minobrnauka) (16.8939.2017/8.9, 2.2267.2017/4.6); Russian Foundation for Basic Research (RFBR) (16-32-00444, 16-37-60076, 16-29-05317, 17-02-01134); Knut och Alice Wallenbergs Stiftelse.

Acknowledgment. Authors acknowledge fruitful discussion with Philippe Tassin, Boris Luk'yanchuk, Andrea Alù, Pavel Belov, and Yuri Kivshar.

†These authors contributed equally to this work.

REFERENCES

1. M. Pelton, J. Aizpurua, and G. Bryant, "Metal nanoparticle plasmonics," Laser Photon. Rev. **2**, 136–159 (2008).
2. J. A. Schuller, E. S. Barnard, W. Cai, Y. C. Jun, J. S. White, and M. L. Brongersma, "Plasmonics for extreme light concentration and manipulation," Nat. Mater. **9**, 193–204 (2010).
3. V. Giannini, A. I. Fernandez-Dominguez, S. C. Heck, and S. A. Maier, "Plasmonic nanoantennas: fundamentals and their use in controlling the radiative properties of nanoemitters," Chem. Rev. **111**, 3888–3912 (2011).
4. X. Fan, W. Zheng, and D. J. Singh, "Light scattering and surface plasmons on small spherical particles," Light Sci. Appl. **3**, e179 (2014).
5. C. M. Soukoulis and M. Wegener, "Past achievements and future challenges in the development of three-dimensional photonic metamaterials," Nat. Photonics **5**, 523–530 (2011).
6. P. Tassin, T. Koschny, M. Kafesaki, and C. M. Soukoulis, "A comparison of graphene, superconductors and metals as conductors for metamaterials and plasmonics," Nat. Photonics **6**, 259–264 (2012).

7. P. R. West, S. Ishii, G. V. Naik, N. K. Emani, V. M. Shalaev, and A. Boltasseva, "Searching for better plasmonic materials," Laser Photon. Rev. **4**, 795–808 (2010).
8. J. B. Khurgin and G. Sun, "Practicality of compensating the loss in the plasmonic waveguides using semiconductor gain medium," App. Phys. Lett. **100**, 11105 (2012).
9. J. B. Khurgin, "How to deal with the loss in plasmonics and metamaterials," Nat. Nanotechnol. **10**, 2–6 (2015).
10. M. Gather, K. Meerholz, N. Danz, and K. Leosson, "Net optical gain in a plasmonic waveguide embedded in a fluorescent polymer," Nat. Photonics **4**, 457–461 (2010).
11. S. Wuestner, A. Pusch, K. L. Tsakmakidis, J. M. Hamm, and O. Hess, "Overcoming losses with gain in a negative refractive index metamaterial," Phys. Rev. Lett. **105**, 127401 (2010).
12. M. I. Stockman, "Spaser action, loss compensation, and stability in plasmonic systems with gain," Phys. Rev. Lett. **106**, 156802 (2011).
13. A. Pusch, S. Wuestner, J. M. Hamm, K. L. Tsakmakidis, O. Hess, M. A. Maxwell-Bloch, A. Pusch, S. Wuestner, J. M. Hamm, K. L. Tsakmakidis, and O. Hess, "Coherent amplification and noise in Langevin approach," ACS Nano **6**, 2420–2431 (2012).
14. A. A. Lisyansky, I. A. Nechepurenko, A. V. Dorofeenko, A. P. Vinogradov, and A. A. Pukhov, "Channel spaser: coherent excitation of one-dimensional plasmons from quantum dots located along a linear channel," Phys. Rev. B **84**, 153409 (2011).
15. E. S. Andrianov, D. G. Baranov, A. A. Pukhov, A. V. Dorofeenko, A. P. Vinogradov, and A. A. Lisyansky, "Loss compensation by spasers in plasmonic systems," Opt. Express **21**, 13467–13478 (2013).
16. J. B. Khurgin and G. Sun, "In search of the elusive lossless metal," Appl. Phys. Lett. **96**, 181102 (2010).
17. G. V. Naik, V. M. Shalaev, and A. Boltasseva, "Alternative plasmonic materials: beyond gold and silver," Adv. Mater. **25**, 3264–3294 (2013).
18. K. Feng, W. Streyer, Y. Zhong, A. Hoffman, and D. Wasserman, "Photonic materials, structures and devices for Reststrahlen optics," Opt. Express **23**, A1418–A1433 (2015).
19. G. Mie, "Beiträge zur optik trüber medien speziell kolloidaler metallösungen," Ann. Phys. **330**, 377–445 (1908).
20. R. Fenollosa, F. Meseguer, and M. Tymczenko, "Silicon colloids: from microcavities to photonic sponges," Adv. Mater. **20**, 95–98 (2008).
21. E. Xifré-Pérez, R. Fenollosa, and F. Meseguer, "Low order modes in microcavities based on silicon colloids," Opt. Express **19**, 3455–3463 (2011).
22. A. B. Evlyukhin, S. M. Novikov, U. Zywietz, R. L. Eriksen, C. Reinhardt, S. I. Bozhevolnyi, and B. N. Chichkov, "Demonstration of magnetic dipole resonances of dielectric nanospheres in the visible region," Nano Lett. **12**, 3749–3755 (2012).
23. A. I. Kuznetsov, A. E. Miroshnichenko, Y. H. Fu, J. Zhang, and B. Luk'yanchuk, "Magnetic light," Sci. Rep. **2**, 492 (2012).
24. U. Zywietz, A. B. Evlyukhin, C. Reinhardt, and B. N. Chichkov, "Laser printing of silicon nanoparticles with resonant optical electric and magnetic responses," Nat. Commun. **5**, 3402 (2014).
25. S. Jahani and Z. Jacob, "All-dielectric metamaterials," Nat. Nanotechnol. **11**, 23–36 (2016).
26. A. I. Kuznetsov, A. E. Miroshnichenko, M. L. Brongersma, Y. S. Kivshar, and B. Lukyanchuk, "Optically resonant dielectric nanostructures," Science **354**, aag2472 (2016).
27. M. S. Wheeler, J. S. Aitchison, and M. Mojahedi, "Three-dimensional array of dielectric spheres with an isotropic negative permeability at infrared frequencies," Phys. Rev. B **72**, 193103 (2005).
28. B. I. Popa and S. A. Cummer, "Compact dielectric particles as a building block for low-loss magnetic metamaterials," Phys. Rev. Lett. **100**, 207401 (2008).
29. J. A. Schuller, R. Zia, T. Taubner, and M. L. Brongersma, "Dielectric metamaterials based on electric and magnetic resonances of silicon carbide particles," Phys. Rev. Lett. **99**, 107401 (2007).
30. J. C. Ginn, I. Brener, D. W. Peters, J. R. Wendt, J. O. Stevens, P. F. Hines, L. I. Basilio, L. K. Warne, J. F. Ihlefeld, P. G. Clem, and M. B. Sinclair, "Realizing optical magnetism from dielectric metamaterials," Phys. Rev. Lett. **108**, 097402 (2012).
31. A. B. Evlyukhin, C. Reinhardt, A. Seidel, B. S. Lukyanchuk, and B. N. Chichkov, "Optical response features of Si-nanoparticle arrays," Phys. Rev. B **82**, 45404 (2010).
32. P. Moitra, B. A. Slovick, W. Li, I. I. Kravchencko, D. P. Briggs, S. Krishnamurthy, and J. Valentine, "Large-scale all-dielectric metamaterial perfect reflectors," ACS Photon. **2**, 692–698 (2015).
33. A. Arbabi, Y. Horie, M. Bagheri, and A. Faraon, "Dielectric metasurfaces for complete control of phase and polarization with subwavelength spatial resolution and high transmission," Nat. Nanotechnol. **10**, 937–943 (2015).
34. M. I. Shalaev, J. Sun, A. Tsukernik, A. Pandey, K. Nikolskiy, and N. M. Litchinitser, "High-efficiency all-dielectric metasurfaces for ultracompact beam manipulation in transmission mode," Nano Lett. **15**, 6261–6266 (2015).
35. M. Khorasaninejad, W. T. Chen, R. C. Devlin, J. Oh, A. Y. Zhu, and F. Capasso, "Metalenses at visible wavelengths: diffraction-limited focusing and subwavelength resolution imaging," Science **352**, 1190–1194 (2016).
36. Y. F. Yu, A. Y. Zhu, R. Paniagua-Domínguez, Y. H. Fu, B. Luk'yanchuk, and A. I. Kuznetsov, "High-transmission dielectric metasurface with 2π phase control at visible wavelengths," Laser Photon. Rev. **9**, 412–418 (2015).
37. B. Rolly, B. Bebey, S. Bidault, B. Stout, and N. Bonod, "Promoting magnetic dipolar transition in trivalent lanthanide ions with lossless Mie resonances," Phys. Rev. B **85**, 245432 (2012).
38. P. Albella, M. A. Poyli, M. K. Schmidt, S. A. Maier, F. Moreno, J. J. Saenz, and J. Aizpurua, "Low-loss electric and magnetic field-enhanced spectroscopy with subwavelength silicon dimers," J. Phys. Chem. C **117**, 13573–13584 (2013).
39. P. A. Dmitriev, D. G. Baranov, V. A. Milichko, S. V. Makarov, I. S. Mukhin, A. K. Samusev, A. E. Krasnok, P. A. Belov, and Y. S. Kivshar, "Resonant Raman scattering from silicon nanoparticles enhanced by magnetic response," Nanoscale **8**, 9721–9726 (2016).
40. A. Krasnok, S. Glybovski, M. Petrov, S. Makarov, R. Savelev, P. Belov, C. Simovski, and Y. Kivshar, "Demonstration of the enhanced Purcell factor in all-dielectric structures," Appl. Phys. Lett. **108**, 211105 (2016).
41. A. E. Krasnok, A. E. Miroshnichenko, P. A. Belov, and Y. S. Kivshar, "All-dielectric optical nanoantennas," Opt. Express **20**, 20599–20604 (2012).
42. A. García-Etxarri, R. Gómez-Medina, L. S. Froufe-Pérez, C. López, L. Chantada, F. Scheffold, J. Aizpurua, M. Nieto-Vesperinas, and J. J. Sáenz, "Strong magnetic response of submicron silicon particles in the infrared," Opt. Express **19**, 4815–4826 (2011).
43. J. M. Geffrin, B. García-Cámara, R. Gómez-Medina, P. Albella, L. S. Froufe-Pérez, C. Eyraud, A. Litman, R. Vaillon, F. González, M. Nieto-Vesperinas, J. J. Sáenz, and F. Moreno, "Magnetic and electric coherence in forward- and back-scattered electromagnetic waves by a single dielectric subwavelength sphere," Nat. Commun. **3**, 1171 (2012).
44. A. B. Evlyukhin, R. L. Eriksen, W. Cheng, J. Beermann, C. Reinhardt, A. Petrov, S. Prorok, M. Eich, B. N. Chichkov, and S. I. Bozhevolnyi, "Optical spectroscopy of single Si nanocylinders with magnetic and electric resonances," Sci. Rep. **4**, 4126 (2014).
45. P. Albella, T. Shibanuma, and S. A. Maier, "Switchable directional scattering of electromagnetic radiation with subwavelength asymmetric silicon dimers," Sci. Rep. **5**, 18322 (2015).
46. Y. H. Fu, A. I. Kuznetsov, A. E. Miroshnichenko, Y. F. Yu, and B. Luk'yanchuk, "Directional visible light scattering by silicon nanoparticles," Nat. Commun. **4**, 1527 (2013).
47. R. S. Savelev, S. V. Makarov, A. E. Krasnok, and P. A. Belov, "From optical magnetic resonance to dielectric nanophotonics (a review)," Opt. Spectrosc. **119**, 551–568 (2015).
48. S. V. Li, D. G. Baranov, A. E. Krasnok, and P. A. Belov, "All-dielectric nanoantennas for unidirectional excitation of electromagnetic guided modes," Appl. Phys. Lett. **107**, 171101 (2015).
49. D. Markovich, K. Baryshnikova, A. Shalin, A. Samusev, A. Krasnok, and P. Belov, "Enhancement of artificial magnetism via resonant bianisotropy," Sci. Rep. **6**, 22546 (2016).
50. M. R. Shcherbakov, D. N. Neshev, B. Hopkins, A. S. Shorokhov, I. Staude, E. V. Melik-Gaykazyan, M. Decker, A. A. Ezhov, A. E. Miroshnichenko, I. Brener, A. A. Fedyanin, and Y. S. Kivshar, "Enhanced third-harmonic generation in silicon nanoparticles driven by magnetic response," Nano Lett. **14**, 6488–6492 (2014).
51. S. Makarov, S. Kudryashov, I. Mukhin, A. Mozharov, V. Milichko, A. Krasnok, and P. Belov, "Tuning of magnetic optical response in a dielectric nanoparticle by ultrafast photoexcitation of dense electron-hole plasma," Nano Lett. **15**, 6187–6192 (2015).
52. M. R. Shcherbakov, P. P. Vabishchevich, A. S. Shorokhov, K. E. Chong, D.-Y. Choi, I. Staude, A. E. Miroshnichenko, D. N. Neshev, A. A. Fedyanin, and Y. S. Kivshar, "Ultrafast all-optical switching with

magnetic resonances in nonlinear dielectric nanostructures," Nano Lett. **15**, 6985–6990 (2015).
53. D. G. Baranov, S. V. Makarov, V. A. Milichko, S. I. Kudryashov, A. E. Krasnok, and P. A. Belov, "Nonlinear transient dynamics of photoexcited resonant silicon nanostructures," ACS Photon. **3**, 1546–1551 (2016).
54. I. Staude and J. Schilling, "Metamaterial-inspired silicon nanophotonics," Nat. Photonics **11**, 274–284 (2017).
55. S. A. Maier, "Plasmonic field enhancement and SERS in the effective mode volume picture," Opt. Express **14**, 1957–1964 (2006).
56. P. Bharadwaj, B. Deutsch, and L. Novotny, "Optical antennas," Adv. Opt. Photon. **1**, 438–483 (2009).
57. M. Agio, "Optical antennas as nanoscale resonators," Nanoscale **4**, 692–706 (2012).
58. T. J. Seok, A. Jamshidi, M. Kim, S. Dhuey, A. Lakhani, H. Choo, P. J. Schuck, S. Cabrini, A. M. Schwartzberg, J. Bokor, E. Yablonovitch, and M. C. Wu, "Radiation engineering of optical antennas for maximum field enhancement," Nano Lett. **11**, 2606–2610 (2011).
59. X. Zambrana-Puyalto and N. Bonod, "Purcell factor of spherical Mie resonators," Phys. Rev. B **91**, 195422 (2015).
60. D. Smirnova and Y. Kivshar, "Multipolar nonlinear nanophotonics," Optica **3**, 1241 (2016).
61. C. F. Klingshirn, *Semiconductor Optics* (Springer, 2012).
62. P. Y. Yu and M. Cardona, *Fundamentals of Semiconductors* (Springer, 2010).
63. H. M. Nussenzveig, *Causality and Dispersion Relations* (Academic, 1972).
64. J. D. Caldwell, L. Lindsay, V. Giannini, I. Vurgaftman, T. L. Reinecke, S. A. Maier, and O. J. Glembocki, "Low-loss, infrared and terahertz nanophotonics using surface phonon polaritons," Nanophotonics **4**, 44 (2015).
65. T. S. Moss, "Relations between the refractive index and energy gap of semiconductors," Phys. Status Solidi B **131**, 415–427 (1985).
66. N. Ravindra, P. Ganapathy, and J. Choi, "Energy gap-refractive index relations in semiconductors-an overview," Infrared Phys. Technol. **50**, 21–29 (2006).
67. P. Herve and L. Vandamme, "General relation between refractive index and energy gap in semiconductors," Infrared Phys. Technol. **35**, 609–615 (1994).
68. M. A. Green and M. J. Keevers, "Optical properties of intrinsic silicon at 300 k," Prog. Photovoltaics **3**, 189–192 (1995).
69. H. Li, "Refractive index of silicon and germanium and its wavelength and temperature derivatives," J. Phys. Chem. Ref. Data **9**, 561–658 (1980).
70. D. Pierce and W. Spicer, "Electronic structure of amorphous Si from photoemission and optical studies," Phys. Rev. B **5**, 3017–3029 (1972).
71. G. Jellison, "Optical functions of GaAs, GaP, and Ge determined by two-channel polarization modulation ellipsometry," Opt. Mater. **1**, 151–160 (1992).
72. D. Aspnes and A. Studna, "Dielectric functions and optical parameters of Si, Ge, GaP, GaAs, GaSb, InP, InAs, and InSb from 1.5 to 6.0 ev," Phys. Rev. B **27**, 985–1009 (1983).
73. J. R. DeVore, "Refractive indices of rutile and sphalerite," J. Opt. Soc. Am. **41**, 416–419 (1951).
74. E. D. Palik, *Handbook of Optical Constants of Solids* (Academic, 1998).
75. R. Ferrini, M. Patrini, and S. Franchi, "Optical functions from 0.02 to 6 ev of $Al_xGa_{1-x}Sb$/GaSb epitaxial layers," J. Appl. Phys. **84**, 4517–4524 (1998).
76. R. S. Caldwell and H. Fan, "Optical properties of tellurium and selenium," Phys. Rev. **114**, 664–675 (1959).
77. F. Weiting and Y. Yixun, "Temperature effects on the refractive index of lead telluride and zinc selenide," Infrared Phys. **30**, 371–373 (1990).
78. C. Okoye, "Electronic and optical properties of snte and gete," J. Phys. Condens. Matter **14**, 8625–8637 (2002).
79. J. I. Larruquert, A. P. Pérez-Marín, S. García-Cortés, L. Rodríguez-de Marcos, J. A. Aznárez, and J. A. Méndez, "Self-consistent optical constants of SiC thin films," J. Opt. Soc. Am. A **28**, 2340–2345 (2011).
80. U. Zywietz, M. Schmidt, A. Evlyukhin, C. Reinhardt, J. Aizpurua, and B. Chichkov, "Electromagnetic resonances of silicon nanoparticle dimers in the visible," ACS Photon. **2**, 913–920 (2015).
81. S. Campione, S. Liu, L. I. Basilio, L. K. Warne, W. L. Langston, T. S. Luk, J. R. Wendt, J. L. Reno, G. A. Keeler, I. Brener, and M. B. Sinclair, "Broken symmetry dielectric resonators for high quality factor Fano metasurfaces," ACS Photon. **3**, 2362–2367 (2016).
82. J. Fan and P. Chu, "Group IV nanoparticles: synthesis, properties, and biological applications," Small **6**, 2080–2098 (2010).
83. K. Tamarov, L. Osminkina, S. Zinovyev, K. Maximova, J. Kargina, M. Gongalsky, Y. Ryabchikov, A. Al-Kattan, A. Sviridov, M. Sentis, A. Ivanov, V. Nikiforov, A. Kabashin, and V. Timoshenko, "Radio frequency radiation-induced hyperthermia using Si nanoparticle-based sensitizers for mild cancer therapy," Sci. Rep. **4**, 7034 (2014).
84. P. Blandin, K. Maximova, M. Gongalsky, J. Sanchez-Royo, V. Chirvony, M. Sentis, V. Timoshenko, and A. Kabashin, "Femtosecond laser fragmentation from water-dispersed microcolloids: toward fast controllable growth of ultrapure Si-based nanomaterials for biological applications," J. Mater. Chem. B **1**, 2489–2495 (2013).
85. L. Gu, D. Hall, Z. Qin, E. Anglin, J. Joo, D. Mooney, S. Howell, and M. Sailor, "*In vivo* time-gated fluorescence imaging with biodegradable luminescent porous silicon nanoparticles," Nat. Commun. **4**, 2326 (2013).
86. R. Kormer, B. Butz, E. Spiecker, and W. Peukert, "Crystal shape engineering of silicon nanoparticles in a thermal aerosol reactor," Cryst. Growth Des. **12**, 1330–1336 (2012).
87. M. van de Haar, J. van de Groep, B. Brenny, and A. Polman, "Controlling magnetic and electric dipole modes in hollow silicon nanocylinders," Opt. Express **24**, 2047–2064 (2016).
88. E.-K. Lee, J.-H. Song, K.-Y. Jeong, J.-H. Kang, H.-G. Park, and M.-K. Seo, "Resonant light scattering from a single dielectric nano-antenna formed by electron beam-induced deposition," Sci. Rep. **5**, 10400 (2015).
89. J. Feng, Q. Li, and S. Fan, "Compact and low cross-talk silicon-on-insulator crossing using a periodic dielectric waveguide," Opt. Lett. **35**, 3904–3906 (2010).
90. I. Staude, A. E. Miroshnichenko, M. Decker, N. T. Fofang, S. Liu, E. Gonzales, J. Dominguez, T. S. Luk, D. N. Neshev, I. Brener, and Y. Kivshar, "Tailoring directional scattering through magnetic and electric resonances in subwavelength silicon nanodisks," ACS Nano **7**, 7824–7832 (2013).
91. P. Spinelli, M. Verschuuren, and A. Polman, "Broadband omnidirectional antireflection coating based on subwavelength surface Mie resonators," Nat. Commun. **3**, 692 (2012).
92. R. Verre, L. Shao, N. O. Länk, P. Karpinski, A. B. Yankovich, T. J. Antosiewicz, E. Olsson, and M. Käll, "Metasurfaces and colloidal suspensions composed of 3D chiral Si nanoresonators," Adv. Mater. (2017).
93. S. Person, M. Jain, Z. Lapin, J. J. Saenz, G. Wicks, and L. Novotny, "Demonstration of zero optical backscattering from single nanoparticles," Nano Lett. **13**, 1806–1809 (2013).
94. S. Liu, M. B. Sinclair, S. Saravi, G. A. Keeler, Y. Yang, J. Reno, G. M. Peake, F. Setzpfandt, I. Staude, T. Pertsch, and I. Brener, "Resonantly enhanced second-harmonic generation using III-V semiconductor all-dielectric metasurfaces," Nano Lett. **16**, 5426–5432 (2016).
95. M. Shcherbakov, S. Liu, V. Zubyuk, A. Vaskin, P. Vabishchevich, G. Keeler, T. Pertsch, T. Dolgova, I. Staude, I. Brener, and A. Fedyanin, "Ultrafast all-optical tuning of direct-gap semiconductor metasurfaces," Nat. Commun. **8**, 1 (2017).
96. S. Liu, G. A. Keeler, J. L. Reno, M. B. Sinclair, and I. Brener, "III-V semiconductor nanoresonators-a new strategy for passive, active and nonlinear all-dielectric metamaterials," Adv. Opt. Mater. **4**, 1457–1462 (2016).
97. S. Liu, J. F. Ihlefeld, J. Dominguez, E. F. Gonzales, J. E. Bower, D. B. Burckel, M. B. Sinclair, and I. Brener, "Realization of tellurium-based all dielectric optical metamaterials using a multi-cycle deposition-etch process," Appl. Phys. Lett. **102**, 161905 (2013).
98. P. Spinelli, B. Macco, M. A. Verschuuren, W. Kessels, and A. Polman, "Al_2O_3/TiO_2 nano-pattern antireflection coating with ultralow surface recombination," Appl. Phys. Lett. **102**, 233902 (2013).
99. R. C. Devlin, M. Khorasaninejad, W. T. Chen, J. Oh, and F. Capasso, "Broadband high-efficiency dielectric metasurfaces for the visible spectrum," Proc. Natl. Acad. Sci. USA **113**, 10473–10478 (2016).
100. P. Genevet, F. Capasso, F. Aieta, M. Khorasaninejad, and R. Devlin, "Recent advances in planar optics: from plasmonic to dielectric metasurfaces," Optica **4**, 139–152 (2017).
101. M. Decker and I. Staude, "Resonant dielectric nanostructures: a low-loss platform for functional nanophotonics," J. Opt. **18**, 103001 (2016).
102. L. Shi, T. Tuzer, R. Fenollosa, and F. Meseguer, "A new dielectric metamaterial building block with a strong magnetic response in the sub-1.5-micrometer region: silicon colloid nanocavities," Adv. Mater. **24**, 5934–5938 (2012).

103. W. O'Mara, R. B. Herring, and L. P. Hunt, *Handbook of Semiconductor Silicon Technology* (Noyes, 1990).
104. J. Proust, F. Bedu, S. Chenot, I. Soumahoro, I. Ozerov, B. Gallas, R. Abdeddaim, and N. Bonod, "Chemical alkaline etching of silicon Mie particles," Adv. Opt. Mater. **3**, 1280–1286 (2015).
105. L. Shi, J. Harris, R. Fenollosa, I. Rodriguez, X. Lu, B. Korgel, and F. Meseguer, "Monodisperse silicon nanocavities and photonic crystals with magnetic response in the optical region," Nat. Commun. **4**, 1904 (2013).
106. S. J. Kim, I. Thomann, J. Park, J.-H. Kang, A. P. Vasudev, and M. L. Brongersma, "Light trapping for solar fuel generation with Mie resonances," Nano Lett. **14**, 1446–1452 (2014).
107. M. Abbarchi, M. Naffouti, B. Vial, A. Benkouider, L. Lermusiaux, L. Favre, A. Ronda, S. Bidault, I. Berbezier, and N. Bonod, "Wafer scale formation of monocrystalline silicon-based Mie resonators via silicon-on-insulator dewetting," ACS Nano **8**, 11181–11190 (2014).
108. T. Wood, M. Naffouti, J. Berthelot, T. David, J.-B. Claude, L. Metayer, A. Delobbe, L. Favre, A. Ronda, I. Berbezier, N. Bonod, and M. Abbarchi, "All-dielectric color filters using SiGe-based Mie resonator arrays," ACS Photon. **4**, 873–883 (2017).
109. T. Lewi, H. A. Evans, N. A. Butakov, and J. A. Schuller, "Ultrawide thermo-optic tuning of PbTe meta-atoms," Nano Lett. **17**, 3940–3945 (2017).
110. T.-J. Zhu, X. Chen, Y.-Q. Cao, and X.-B. Zhao, "Controllable synthesis and shape evolution of PbTe three-dimensional hierarchical superstructures via an alkaline hydrothermal method," J. Phys. Chem. C **113**, 8085–8091 (2009).
111. J. Ye and C. Thompson, "Templated solid-state dewetting to controllably produce complex patterns," Adv. Mater. **23**, 1567–1571 (2011).
112. C. V. Thompson, "Solid-state dewetting of thin films," Annu. Rev. Mater. Res. **42**, 399–434 (2012).
113. M. Naffouti, T. David, A. Benkouider, L. Favre, A. Ronda, I. Berbezier, S. Bidault, N. Bonod, and M. Abbarchi, "Fabrication of poly-crystalline Si-based Mie resonators via amorphous Si on SiO_2 dewetting," Nanoscale **8**, 2844–2849 (2016).
114. E. Weidmann and J. Anderson, "Structure and growth of oriented tellurium thin films," Thin Solid Films **7**, 265–276 (1971).
115. P. Zhang, B. Yang, P. Rugheimer, M. Roberts, D. Savage, F. Liu, and M. Lagally, "Influence of germanium on thermal dewetting and agglomeration of the silicon template layer in thin silicon-on-insulator," J. Phys. D **42**, 175309 (2009).
116. J. Yan, P. Liu, Z. Lin, H. Wang, H. Chen, C. Wang, and G. Yang, "Magnetically induced forward scattering at visible wavelengths in silicon nanosphere oligomers," Nat. Commun. **6**, 7042 (2015).
117. S. Okamoto, K. Inaba, T. Iida, H. Ishihara, S. Ichikawa, and M. Ashida, "Fabrication of single-crystalline microspheres with high sphericity from anisotropic materials," Sci. Rep. **4**, 5186 (2014).
118. P. Dmitriev, S. Makarov, V. Milichko, I. Mukhin, A. Gudovskikh, A. Sitnikova, A. Samusev, A. Krasnok, and P. Belov, "Laser fabrication of crystalline silicon nanoresonators from an amorphous film for low-loss all-dielectric nanophotonics," Nanoscale **8**, 5043–5048 (2015).
119. T. Schwarz-Selinger, D. G. Cahill, S.-C. Chen, S.-J. Moon, and C. Grigoropoulos, "Micron-scale modifications of Si surface morphology by pulsed-laser texturing," Phys. Rev. B **64**, 155323 (2001).
120. U. Zywietz, C. Reinhardt, A. Evlyukhin, T. Birr, and B. Chichkov, "Generation and patterning of Si nanoparticles by femtosecond laser pulses," Appl. Phys. A **114**, 45–50 (2014).
121. T. Lewi, P. P. Iyer, N. A. Butakov, A. A. Mikhailovsky, and J. A. Schuller, "Widely tunable infrared antennas using free carrier refraction," Nano Lett. **15**, 8188–8193 (2015).
122. J. Bohandy, B. Kim, F. Adrian, and A. Jette, "Metal deposition at 532 nm using a laser transfer technique," J. Appl. Phys. **63**, 1158–1162 (1988).
123. J.-H. Yoo, J. In, C. Zheng, I. Sakellari, R. Raman, M. Matthews, S. Elhadj, and C. Grigoropoulos, "Directed dewetting of amorphous silicon film by a donut-shaped laser pulse," Nanotechnology **26**, 165303 (2015).
124. Q. D. Gibson, L. M. Schoop, L. Muechler, L. S. Xie, M. Hirschberger, N. P. Ong, R. Car, and R. J. Cava, "Three-dimensional dirac semimetals: design principles and predictions of new materials," Phys. Rev. B **91**, 205128 (2015).
125. T. Wehling, A. Black-Schaffer, and A. Balatsky, "Dirac materials," Adv. Phys. **63**, 1–76 (2014).
126. H. Weng, X. Dai, and Z. Fang, "Topological semimetals predicted from first-principles calculations," J. Phys. Condens. Matter **28**, 303001 (2016).